The effects of introducing elasticity using different interpolation schemes to the grand potential phase field model

Pierre-Clément A. Simon[a,*], Larry K. Aagesen[b], Arthur T. Motta[a], Michael R. Tonks[c]

[a] *Ken and Mary Alice Lindquist Department of Nuclear Engineering, The Pennsylvania State University, University Park, PA 16802, USA*
[b] *Computational Mechanics and Materials Department, Idaho National Laboratory, Idaho Falls, ID 83415, USA*
[c] *Department of Materials Science and Engineering, University of Florida, Gainesville, FL 32611, USA*

ABSTRACT

Introducing elastic energy in the phase field method has been shown to influence interfacial energy, depending on the elastic interpolation scheme. This study investigates the impact of the elastic energy when using a grand potential-based phase field method, comparing the result of Khachaturyan's strain interpolation scheme (KHS) and Voight-Taylor's elastic energy interpolation scheme (VTS). The KHS model leads to a decrease in the interfacial energy, while the VTS model leads to an increase. The change in interfacial energy is greater with the VTS model than the KHS model, which suggests that the KHS model is more appropriate to limit the artificial impact of the elastic energy on the interfacial energy. When the contribution at the interface is not negligible, it is shown that both the microstructure evolution kinetics and the equilibrium microstructure can be influenced by the choice of the elastic scheme being used. In addition, this paper shows that the grand potential model might not be appropriate when the system requires the introduction of a composition-dependent term in the elastic energy contribution. This limitation is due to the need for an explicit and invertible relation between the total potential and the composition.

1. Introduction

Phase field modeling has been widely used for the study of microstructure evolution [1–3]. It allows quantitative coupling of several physics, such as thermodynamics, mechanical deformation, and plastic deformation. As a result, it has been used in a wide range of applications, including solid-state phase transformation [1], grain growth [4–6], crack propagation [7–9], and numerous other phenomena [10,11]. It can be a powerful tool for material discoveries at the mesoscale [12]. Phase field modeling is based on a continuous description of the microstructure, resulting in diffuse interfaces.

One limitation of some phase field models is the intrinsic coupling between the bulk free energy of the different phases of the system and the interfacial free energy. In the commonly used approach from Wheeler, Boettinger, and McFadden (WBM model) [13], this coupling causes the interfacial energy to be a function of the interface thickness. This constraint on the interfacial thickness leads to strict requirements on the mesh size, which directly impacts computational costs and makes the simulation of large microstructures challenging. The grand potential model is an alternative phase field model that, with some assumptions, defines the interfacial thickness independently of the bulk

and interfacial free energies [14–22]. As such, the interface can be defined larger in the grand potential model than in the WBM model, thus reducing computational costs. The phase field approach developed by Kim, Kim, and Suzuki (KKS) [23] also decouples the bulk and interfacial free energies and reduces computational costs compared with the WBM model. However, the grand potential model has a lower computational and memory costs than the KKS model, as it does not require tracking phase concentrations and has a smaller system of equations. Assuming the assumptions required by the grand potential model are satisfied, the grand potential model is expected to offer lower computational costs than other phase field approaches.

As phase field models are applied to a wide variety of multi-physics systems, adding the contribution of the elastic energy in the phase field model is often crucial to obtain a quantitative description of the microstructure's evolution. However, the introduction of an elastic model can impact the interfacial energy of the system by adding an excess elastic energy contribution at the interface, artificially increasing or decreasing the interfacial energy of the system [24–26]. The Voight-Taylor scheme (VTS) [27] and the Khachaturyan scheme (KHS) [28,29] are the two different elastic schemes compared in this study. Other elastic schemes, such as the Steinbach-Apel's scheme (SAS) [30], more

---

sophisticated versions of the KHS scheme [31,32], or recently developed schemes combining the VTS and SAS schemes [24,25] have not been introduced in this work. The difference between the VTS and KHS models resides in the interpolation of the elastic properties across the interface. The objectives of this study are to quantify the excess elastic energy introduced in the system for different interfacial thicknesses, quantify the effect of this excess energy on microstructure evolution, and compare the performance of the two elastic schemes when coupled with the grand potential model. Similar comparisons of the performance of the KHS and the VTS schemes have been done in the context of the phase field approach developed by Kim, Kim, and Suzuki (KKS) and have found that both elastic schemes introduced an excess elastic energy at the interface [24,26]. However, to the authors' knowledge, this study is the first to focus on the effects of the different schemes on microstructure evolution in the context of the grand potential model. As the description of the interface differs between the KKS and grand potential model, the results obtained when coupling the KKS model with the elastic schemes cannot be extended to the grand potential model, which motivated this study.

The grand potential model and elastic schemes are described in Section 2. The performances of the two elastic schemes are first compared in Section 3 with an analytical solution in one 2D rectangular configuration, and another 3D circular inclusion configuration with a cylindrical symmetry. The excess elastic contribution introduced by both schemes is determined, and the effect of interfacial thickness on the magnitude of this excess is quantified. The effect of the excess elastic energy introduced at the interface by the elastic schemes on microstructure evolution is then investigated in Section 4 to show how the choice of elastic scheme can influence the results of a study.

In addition, in Section 5, this paper explains how the assumptions made for the development of the grand potential model restrains the introduction of a concentration-dependent term in addition to the chemical free energy in the total energy functional.

2. Grand potential model coupled with elasticity

When using the grand potential model to study a system composed of N phases (α, β, …), with P_α crystallographic orientations for each phase ($i = 1…P_\alpha$), the properties of the system are defined by the grand potential functional [26,14]

$$\Omega = \int_V (\omega_{bulk} + \omega_{grad} + \omega_{chem+el})dV. \tag{1}$$

ω_{bulk} represents the bulk grand potential density [5]

$$\omega_{bulk} = m\left(\sum_\alpha \sum_{i=1}^{P_\alpha} \left(\frac{\eta_{\alpha_i}^4}{4} - \frac{\eta_{\alpha_i}^2}{2}\right) + \sum_\alpha \sum_{i=1}^{P_\alpha} \left[\sum_\beta \sum_{j=1,\beta_j \neq \alpha_i}^{P_\beta} \frac{\gamma_{\alpha_i\beta_j}}{2}\eta_{\alpha_i}^2\eta_{\beta_j}^2\right] + \frac{1}{4}\right), \tag{2}$$

with m scaling the value of the bulk grand potential, and $\gamma_{\alpha_i\beta_j}$ contributing to the interfacial energy between the orientation i of phase α and the orientation j of phase β. $\gamma_{\alpha_i\beta_j}$ can have significant effects on the properties of ω_{bulk} and on the shape and orientation of the interfaces, in particular on triple junctions [5,33,34]. In this study, to ensure symmetrical interfaces and ease comparison with analytical solutions, $\gamma_{\alpha_i\beta_j}$ is fixed to 1.5 [5].

ω_{grad} corresponds to the contribution of the gradient of the order parameters to the grand potential density

$$\omega_{grad} = \frac{\kappa}{2} \sum_\alpha \sum_{i=1}^{P_\alpha} |\nabla\eta_{\alpha_i}|^2, \tag{3}$$

where κ is the gradient energy coefficient, and is assumed to be independent of the composition and the interface orientation in this model.

ω_{bulk} and ω_{grad} define the interfacial thickness and the interfacial energy of the system. Moelans et al. [5] provide the expression of the interfacial energies

$$\sigma_{\alpha_i\beta_j} = \frac{1}{3}\sqrt{m\kappa\left(\frac{1}{2} + \gamma_{\alpha_i\beta_j}\right)}, \tag{4}$$

and the interfacial thicknesses

$$l_{\alpha_i\beta_j} = \sqrt{\frac{\kappa}{m\omega_{bulk,interf}}}, \tag{5}$$

as functions of the parameters m, $\gamma_{\alpha_i\beta_j}$, and κ in the absence of elastic contribution. $\omega_{bulk,interf} = \frac{2\gamma_{\alpha_i\beta_j} - 1}{4(2\gamma_{\alpha_i\beta_j} + 1)}$ is the bulk grand potential density at the saddle point [5].

The term $\omega_{chem+el}$ from Eq. (1) describes the grand potential density of the contributions from the chemical free energy and the elastic free energy. $\omega_{chem+el}$ is the Legendre transform of the free energy $f_{chem+el}$, which is equal to the sum of the chemical free energy f_{chem} and the elastic free energy f_{el}. $\omega_{chem+el}$ is hence defined as

$$\omega_{chem+el} = f_{chem+el} - \mu\rho = f_{chem} + f_{el} - \mu\rho, \tag{6}$$

with μ the total potential, and $\rho = -\frac{\partial\Omega(\eta,\mu)}{\partial\mu}$ the solute density. f_{chem} is defined as

$$f_{chem} = \sum_\alpha h_\alpha f_\alpha, \tag{7}$$

where h_α are the interpolation functions described in [35] as

$$h_\alpha = \frac{\sum_{i=1}^{P_\alpha} \eta_{\alpha_i}^2}{\sum_\beta \sum_{j=1}^{P_\beta} \eta_{\beta_j}^2}, \tag{8}$$

and f_α are the Helmholtz free energy densities of the different phases. Using the interpolation functions described in [35] ensures that the total weight of the phase free energy contributions is equal to 1 since $\sum_\alpha h_\alpha = 1$. It thus has the advantage of not needing an additional penalty to ensure $\sum_\alpha \eta_\alpha = 1$.

As explained by Plapp in [14], and detailed later in Section 5, convex Helmholtz free energies and concentration-independent elastic contribution ensure the required implicit and invertible relation between the composition c and the total potential μ. Parabolic functions can be used as an accurate convex approximation of the Helmholtz free energies. The chemical free energies are thus written as

$$f_\alpha(x) = \frac{1}{2}k_\alpha(x - x_\alpha^v)^2 + f_\alpha^0, \tag{9}$$

with k_α the curvature of the parabola, x_α^v its vertex, and f_α^0 its minimum value. Once the equilibrium concentration x_α^{eq} and x_β^{eq} have been derived from the common tangent, it is possible to approximate the Helmholtz free energies G_α and G_β of a two-phase system using parabolic function by solving

$$f_\nu(x_\nu^{eq}) = G_\nu(x_\nu^{eq}), \tag{10}$$

$$\frac{\partial f_\nu}{\partial x}(x_\nu^{eq}) = \frac{\partial G_\nu}{\partial c}(x_\nu^{eq}), \tag{11}$$

and

$$\frac{\partial^2 f_\nu}{\partial x^2}(c_\nu^{eq}) = \frac{\partial^2 G_\nu}{\partial x^2}(x_\nu^{eq}) \tag{12}$$

for $\nu = \alpha$ and β. The advantage of this approximation is that the equilibrium concentrations, the common tangent, and the second derivatives of the free energies around the equilibrium concentrations are the same than with the Helmholtz free energies.

As described in Section 5, in the case of parabolic chemical free energies and concentration-independent elastic free energies, the concentration in phase α can be derived from the total potential using [14]

$$x_\alpha = V_a \rho = x_\alpha^v + \frac{\mu}{V_a k_\alpha}, \tag{13}$$

with V_a the atomic volume, assumed constant across phases.

Finally, the elastic free energy f_{el} depends on the elastic scheme being used. In this study, the VTS [27] and KHS [28] elastic schemes are compared. The difference between the two models lies in the interpolation of the material properties at the interface. In the VTS model, the stress and strain are determined separately in each phase, where the elastic energy is then derived. Only then is the global free elastic energy defined as the interpolation of all the elastic free energies

$$f_{el}^{VTS} = \sum_\alpha h_\alpha f_{el,\alpha}^{VTS} = \sum_\alpha h_\alpha \frac{1}{2} C_{ijkl,\alpha}^{VTS} \epsilon_{ij,\alpha}^{VTS} \epsilon_{kl,\alpha}^{VTS}. \tag{14}$$

In the KHS model, the stiffness tensor and the misfit strain are interpolated to create a global stiffness tensor

$$C_{ijkl}^{KHS} = \sum_\alpha h_\alpha C_{ijkl,\alpha}, \tag{15}$$

and a global elastic strain

$$\epsilon_{ij}^{KHS} = \epsilon_{ij}^{tot} - \sum_\alpha h_\alpha \epsilon_{ij,\alpha}^*, \tag{16}$$

where ϵ^{tot} is the total strain and ϵ_α^* is the eigenstrain of phase α. The stress is then determined as a global stress and the contribution of the elastic free energy is derived as

$$f_{el}^{KHS} = \frac{1}{2} C_{ijkl}^{KHS} \epsilon_{ij}^{KHS} \epsilon_{kl}^{KHS}. \tag{17}$$

In both elastic models, the mechanical equilibrium equation is solved assuming a quasi-steady state:

$$\nabla \cdot \sigma_{ij} = 0. \tag{18}$$

The field variables of the grand potential model are the total potential μ and the order parameters η. Plapp describes the derivation of the equations governing the evolution of these field variables [14]. The evolution of the total potential is given by

$$\frac{\partial \mu}{\partial t} = \frac{1}{\chi(\eta, \mu)} \left(\nabla \cdot (D(\eta, \mu) \chi(\eta, \mu) \nabla \mu) - \sum_\alpha \sum_{i=1}^{P_\alpha} \frac{\partial \rho}{\partial \eta_{\alpha_i}} \frac{\partial \eta_{\alpha_i}}{\partial t} \right). \tag{19}$$

The first term on the right hand side is analogous to a diffusion term, while the second term corresponds to the effect of a difference in composition at the interfaces. D is the solute diffusion coefficient and the susceptibility χ is defined as

$$\chi = \frac{\partial \rho}{\partial \mu} = -\frac{\partial^2 \Omega}{\partial \mu^2}. \tag{20}$$

The evolution of the order parameters follows the Allen-Cahn equation [36,23]

$$\frac{\partial \eta_{\alpha_i}}{\partial t} = -L \left[\frac{\partial \Omega}{\partial \eta_{\alpha_i}} \right], \tag{21}$$

where L is a positive kinetic constant that corresponds to the mobility of the interfaces, and Ω is the grand potential functional introduced in Eq. (1).

3. Evaluation of the excess elastic energy

In order to quantify the excess elastic energy introduced in the interface in grand potential models coupled with the KHS and the VTS models, their predictions were compared with analytical solutions for a particular system described in Section 3.1 in different configurations shown in Fig. 1.

Table 1
Constants and parameters used for the verification of the model.

| Constant	Value	Constant	Value
$k_\alpha = k_\beta$	10	V_a	1
$f_\alpha^0 = f_\beta^0$	0	L	1
x_α^{eq}	0.1	D	1
x_β^{eq}	0.9	$\epsilon_{11}^* = \epsilon_{22}^*$	0.01
$\gamma_{\alpha,\beta} = \gamma_{\beta,\alpha}$	1.5	$\epsilon_{33}^* = \epsilon_{23}^* = \epsilon_{13}^* = \epsilon_{12}^*$	0
κ	$\frac{1}{m}$	$C_{11}^\alpha = C_{11}^\beta$	40
$\sigma_{\alpha,\beta}$	$\frac{\sqrt{2}}{3}$	$C_{22}^\alpha = C_{22}^\beta$	40
$l_{\alpha,\beta}$	$\frac{2\sqrt{2}}{m}$	$C_{12}^\alpha = C_{12}^\beta$	20

3.1. System description

The system is composed of two phases: and β. All the parameters and constants of the two-phase system were defined as described in Table 1. κ is defined equal to $\frac{1}{m}$ and $\gamma_{\alpha,\beta} = \gamma_{\beta,\alpha} = 1.5$, such that the interfacial energy $\sigma_{\alpha,\beta}$ is fixed equal to $\frac{\sqrt{2}}{3}$ and the interfacial thickness $l_{\alpha,\beta}$ is equal to $\frac{2\sqrt{2}}{m}$. Varying values of m define different values of the interfacial thickness at a fixed interfacial energy value, which allows studying the effect of the interfacial thickness on the magnitude of the excess elastic energy. To remain general, the system is adimensional.
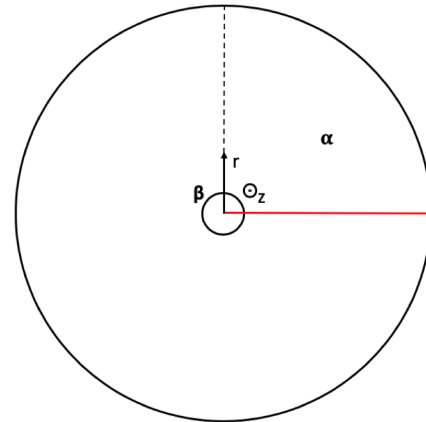
3.2. Configurations

Both configurations represent the two-phase system, one being a rectangular configuration, the other being a 3D circular inclusion configuration with cylindrical symmetry, as shown in Fig. 1.

The rectangle configuration shown in Fig. 1a is shared in half by the α and the β phases. The domain is 100 units of length long and 10/512 wide. A zero-gradient boundary condition is imposed to η_α, η_β, and μ
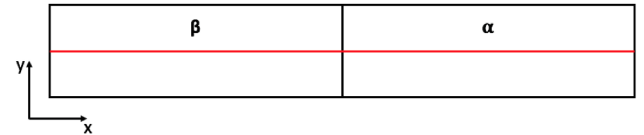
(a) Rectangular configuration

(b) Circular inclusion configuration

Fig. 1. Schematic of the geometry of the domain for the two configurations. (a) is a rectangular configuration, and (b) represents a 3D circular inclusion with cylindrical symmetry. Using these configurations allows verifying the model with two significantly different stress fields. For both configurations, the profile of the results was plotted along the red line.

on all boundaries, while, concerning displacements, $u_x = 0$ on the left and right boundaries, and $u_y = 0$ on the top and bottom boundaries. The initial conditions for the total potential and the order parameters were the equilibrium conditions for an interface ($\eta_\alpha = \eta_\beta = 0.5$) situated in the middle of the domain in the x-direction. Plane strain conditions are imposed.

The domain for the 3D circular inclusion is an infinite cylinder with a radius of $R = 400$. The circular inclusion of β phase is at the center of the domain with a radius equal to $r = 30$, as shown in Fig. 1b. The simulation uses the fact that the cylinder is infinitely long to describe it in 2D, and takes advantage of the cylindrical symmetry of the configuration to further reduce the system's dimension to a 1D line which is shown in red in Fig. 1b. A zero-gradient boundary condition was imposed to η_α, η_β, and μ, while the displacement was defined equal to zero at the center of the circular inclusion, and let free on the outside end. The radius of the domain was defined to be large enough to have almost no displacement due to the inclusion at the edge of the domain. The initial conditions for the total potential and the order parameters were the equilibrium conditions for a circular inclusion in an α matrix. Plane strain conditions are imposed.

3.3. Numerical method

All simulations have been performed using the Multiphysics Object-Oriented Simulation Environment MOOSE [37–40]. The numerical parameters are the same for both elastic schemes to ensure that differences in the models' predictions are exclusively due to the different elastic schemes. For both configurations, the variables are defined as linear Lagrange elements, and equations are solved using a pre-conditionned Jacobian-free Newton-Krylov method and the second-order accurate backward difference formula for time integration. To reduce computational costs, an iteration adaptive time-stepping scheme is used with a number of optimal iterations equal to 5 ± 1 and a maximum of 5 % increase per time step. No mesh adaptivity is introduced in the simulation. In the 2D configuration, the mesh is fixed with one element in the y-direction, and 5120 square elements in the x-direction to resolve the interface. In the 3D circular inclusion, the 1D lined used to simulate the entire domain using cylindrical symmetry is meshed with 5120 elements of equal size to resolve the interface.

3.4. Analytical solutions

The analytical solution used to verify the models consists of expressions for the total strain defined as the sum of the elastic strain and the eigenstrain in Eq. (16), the stress components, and the elastic free energy. The derivations of the analytical solution for the two configurations of interest can be found in several articles [24,26]. To determine the strain, the stress and the elastic free energy, the α phase is taken as a reference and the β phase is compressed to fit the smaller volume of the α phase. The derivation of the analytical solution in the case of the 2D rectangular configuration can be found in [26]. The analytical solution for the 3D circular inclusion is based on the Eshelby solution for a misfit isotropic inclusion derived in [41] and used in [25,26].

3.5. Simulations results and discussion

The profiles of the total strain, stress, and elastic free energy across the domain for the two elastic schemes and the two configurations are provided in Fig. 2. Both the KHS and VTS models accurately predict the total strain (cf. Fig. 2a and b), the stress (cf. Fig. 2c and d), and the elastic energy (cf. Fig. 2e and f) far from the interface. At the interface, the KHS and VTS models provide similar predictions of strain and stress, but differ in their elastic free energy profiles. The profile of the elastic free energy across the interface allows comparing the performances of the different elastic models (cf. Fig. 2e and f). The elastic free

energy of the analytical solution corresponds to an interpolation of the elastic free energy using the order parameter profile obtained without elasticity. Any departure from the profile of elastic energy provided by the analytical solution is referred to as the excess elastic energy. The analytical solution thus presents, by construction, no excess elastic energy. The VTS and KHS models present respectively a positive excess elastic energy with a large peak at the interface and a slightly negative excess elastic free energy. Due to the lower magnitude of the excess elastic energy, the KHS model seems more appropriate than the VTS model for the introduction of the elastic free energy contribution to the grand potential. These observations and this conclusion are consistent with previous studies published by Durga et al. and Aagesen et al. when comparing the VTS and KHS models with different phase field approaches [24,26]. In all cases, the predictions for the stress, strain, and elastic energy were accurate within the phases, and the KHS scheme provided better results than the VTS scheme.

As shown in Fig. 2, the differences between the models' results and the analytical solution lie at the interface. It is important to remember that the strain and stress fields predicted by the analytical solution are derived from a system with sharp interfaces, whereas the grand potential model presents continuous interfaces, which explains the differences in Fig. 2a–d. A convergence study presented in Fig. 3 shows that decreasing the interface thickness of the system reduces the magnitude of the excess free energy. The results were obtained by decreasing the interfacial thickness while keeping a constant interfacial energy. Since for $\gamma = 1.5$, $\sigma = \frac{1}{3}\sqrt{2m\kappa}$ and $l = \sqrt{\frac{8\kappa}{m}}$, one can vary m and κ to change the interface thickness while keeping the interfacial energy constant by ensuring $\kappa = \frac{1}{m}$. Simulations were run until equilibrium for both elastic models for several values of the interfacial thickness ranging from 0.25 to 16 units of length. Then, the excess elastic energy between the simulation results and the analytical solution was defined as the difference between the integral of the elastic energy predicted by the elastic scheme and the analytical elastic energy, as

$$F_{el}^{Excess} = \int_S f_{el}^{Scheme} - f_{el}^{Analytical} \, dS, \tag{22}$$

with F_{el}^{Excess} the excess elastic free energy, f_{el}^{Scheme} the integral over the domain of the elastic free energy derived using the KHS or VTS elastic scheme, and $f_{el}^{Analytical}$ the integral of the elastic free energy derived using the analytical solution.
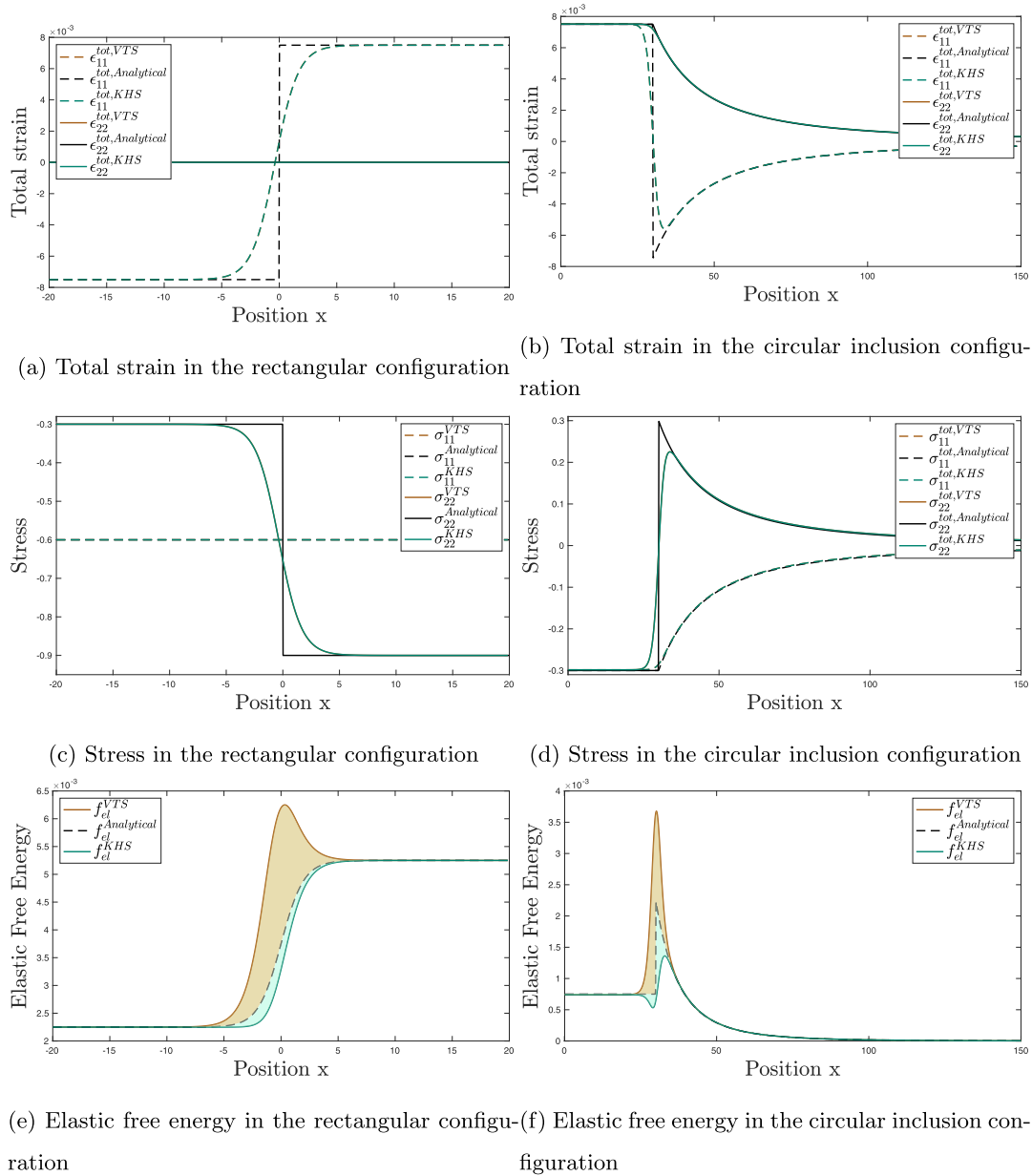
The results for the rectangular configuration are presented in Fig. 3a, and the results for the circular inclusion are provided in Fig. 3b. In both configurations, the figures show that the excess elastic energy between the simulation results and the analytical solution decreases linearly with the interfacial thickness. The result of the convergence study confirms that the differences observed between the models' predictions and the analytical solution at the interface can be limited by using a small interface thickness. The magnitude of the excess elastic energy is lower with the KHS model than with the VTS model.

4. Influence on microstructure evolution

As previously presented, the coupling of a phase field model with an elastic scheme introduces an undesirable excess energy at the interface. The impact of this excess elastic free energy on microstructure evolution is investigated by comparing the results of 2D simulations using an elastic-free grand potential model, as well as grand potential models coupled with the VTS and the KHS schemes. For each model, three simulations are performed with different interfacial lengths to investigate the effect of the magnitude of the excess elastic energy at the interface on the microstructure evolution.

4.1. Model description

The value of the parameters used in the phase field models are presented in Table 2. The contribution of the elastic free energy is

(a) Total strain in the rectangular configuration

(b) Total strain in the circular inclusion configuration

(c) Stress in the rectangular configuration

(d) Stress in the circular inclusion configuration

(e) Elastic free energy in the rectangular configuration

(f) Elastic free energy in the circular inclusion configuration

Fig. 2. Comparison of (a, b) the total strain, (c, d) the stress, and (e,f) the elastic energy density profiles derived using different elastic models (VTS and KHS) with the analytical solution for the (a, c, e) rectangular configuration and the (b,d,f) circular inclusion with an interfacial thickness equal to 8. Both the KHS and VTS models accurately predict the total strain, the stress, and the elastic energy far from the interface. At the interface, the KHS and VTS provide similar predictions of strain and stress, but differ in their elastic free energy profiles. The VTS model overestimates the elastic energy, while the KHS model underestimates it.

linked to the ratio $L^* = \frac{C \, \|\epsilon^*\|^2}{\sigma_{\alpha,\beta}} l_{\alpha,\beta}$ between the elastic constants C, the magnitude of the eigenstrain $\|\epsilon^*\|$, and the interface thickness $l_{\alpha,\beta}$ over the interface energy $\sigma_{\alpha,\beta}$ [26]. C is defined as an appropriate elastic constant and is here defined as $C = (C_{11}^{\beta} + C_{22}^{\beta})/2$ [42,26]. The excess energy contribution thus becomes significant when the elastic constant, the eigenstrain, or the interface thickness are great relative to the interfacial energy. To investigate the effect of the interfacial length, three different systems with $l = 2.5$, $l = 5$, and $l = 10$ are studied for each model. Using the model parameters provided in Table 2, $L^* = 1.06$, $L^* = 2.12$, $L^* = 4.24$ for $l = 2.5$, $l = 5$, $l = 10$, respectively. Since $L^* > 1$ for all systems, the contribution of the excess energy is expected to be significant and increase as the interfacial length increases.

The simulation domain is a 400×400 square with periodic boundary condition for the order parameters η_α and η_β and the total

potential μ. The displacement in the x-direction is periodic in the y-direction, and vice versa. Initially, the order parameters are defined to obtain a microstructure composed of ellipsoids as shown in Fig. 4a and b. The total potential is initially homogeneously equal to $\mu_0 = -0.4$, which means that the system is under-saturated. Both simulations are performed until equilibrium. Plane strain conditions are imposed.

4.2. Numerical method

The numerical parameters are the same for all three models to ensure that differences in the models' predictions are exclusively due to the different elastic schemes. In all simulations, the variables are defined as linear Lagrange elements, and equations are solved using a preconditionned Jacobian-free Newton-Krylov method and the second-order accurate backward difference formula for time integration. To reduce computational costs, an iteration adaptive time-stepping scheme

(a)   (b)
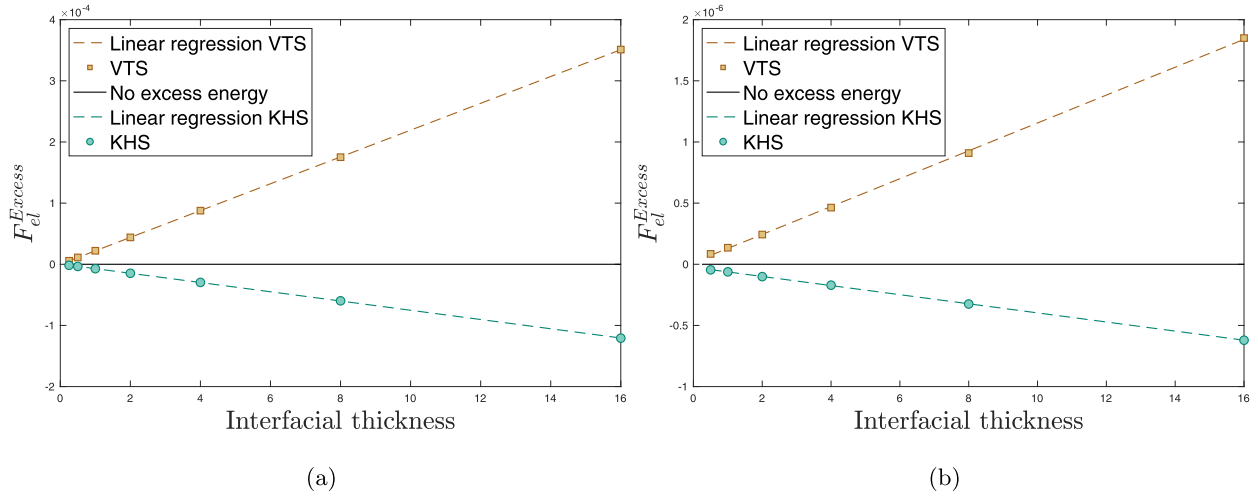
Fig. 3. Evolution of the excess elastic energy F_{el}^{Excess} between the simulation results provided by both the VTS and KHS scheme and the analytical solution for the (a) rectangular configuration and the (b) circular inclusion configuration as a function of the interfacial thickness. The magnitude of the excess elastic energy introduced in the system by the VTS model is consistently greater than for the KHS model. For both models, the excess elastic energy introduced at the interface increases proportionally with the interfacial thickness.

Table 2
Constants and parameters used in the model.

Constant	Value	Constant	Value
$k_\alpha = k_\beta$	10	V_a	1
$f_\alpha^0 = f_\beta^0$	0	L	1
x_α^{eq}	0.1	D	1
x_β^{eq}	0.9	$\epsilon_{11}^* = \epsilon_{22}^*$	0.05
$\gamma_{\alpha,\beta} = \gamma_{\beta,\alpha}$	1.5	$\epsilon_{33}^* = \epsilon_{23}^* = \epsilon_{13}^* = \epsilon_{12}^*$	0
$m = \frac{1}{\kappa}$	$\frac{2\sqrt{2}}{l_{\alpha,\beta}}$	$C_{11}^\alpha = C_{11}^\beta$	40
$\sigma_{\alpha,\beta}$	$\frac{\sqrt{2}}{3}$	$C_{22}^\alpha = C_{22}^\beta$	40
$l_{\alpha,\beta}$	$\frac{2\sqrt{2}}{m} = 2.5, 5, 10$	$C_{12}^\alpha = C_{12}^\beta$	20

is used to increase the initial time step of 1 with a number of optimal iterations equal to 5 ± 1 and a maximum of 5 % increase per time step. However, the maximum time step was fixed at $dt = 50$ to ensure the accuracy of the predictions. Moreover, three levels of mesh adaptivity are introduced to resolve the interface with 5 elements, independently of the interfacial length. For more information, refer to the input files available as research data.

4.3. Results and discussion

Contrasting the predictions of the three different phase field models including no mechanics, the VTS scheme, and the KHS scheme, it appears that microstructure evolution is influenced by the elastic scheme and the interfacial length.

For a given interfacial length, the elastic scheme impacts microstructure evolution and the equilibrium microstructure. As discussed in Section 3, the VTS and the KHS scheme respectively introduce a positive and negative excess elastic energy at the interface. The VTS scheme thus results in quicker kinetics than the KHS model. Fig. 4 shows the microstructure evolution with the VTS and the KHS models for $l = 10$. Despite having the same initial conditions including 6 distinct particles, the microstructure in Fig. 4c predicted by the VTS model contains only 3 particles at time $t = 11723$, while the microstructure in Fig. 4d derived by the KHS model still show 5 particles later, at time $t = 13002$. This difference in kinetics is shown more quantitatively in Fig. 5, which presents the evolution of the number of particles for the elastic free simulations (cf. Fig. 5a and b) as well as the VTS and KHS model (cf.
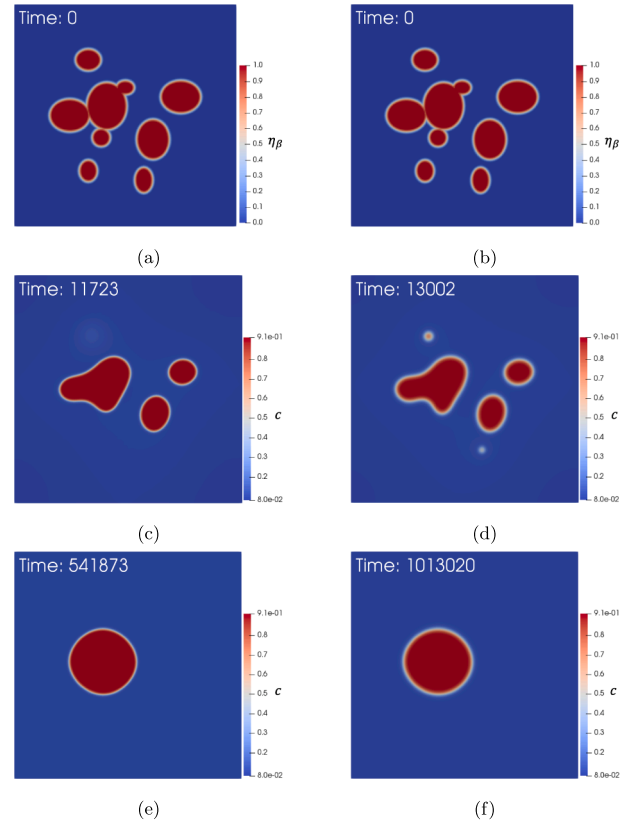
Fig. 4. Evolution of the microstructure when $l = 10$ for (a, c, e) the VTS and (b, d, f) the KHS elastic scheme. The comparison of the microstructures obtained by the two different elastic schemes exposes the possible strong impact of the excess interfacial energy on microstructure evolution, influencing the kinetics of evolution as well as the equilibrium concentrations. The initial conditions are the same for both models (a,b). However, as the system evolves, particles disappear quicker with the VTS model, leading to a microstructure with 3 particles at $t = 11723$ (c), while (d) shows 5 particles at $t = 13002$. In (e) and (f), the equilibrium concentrations are different than $c_{alpha}^{eq} = 0.1$ and $c_{beta}^{eq} = 0.9$. The shifts in equilibrium concentration due to the introduction of elastic energy by the models are different (9.45×10^{-3} for the VTS scheme, 8.65×10^{-3} for the KHS scheme), leading to an equilibrium particle size 5.3% larger for the KHS model than for the VTS model. The domain size is 400×400.

(a)

(b)

(c)

(d)
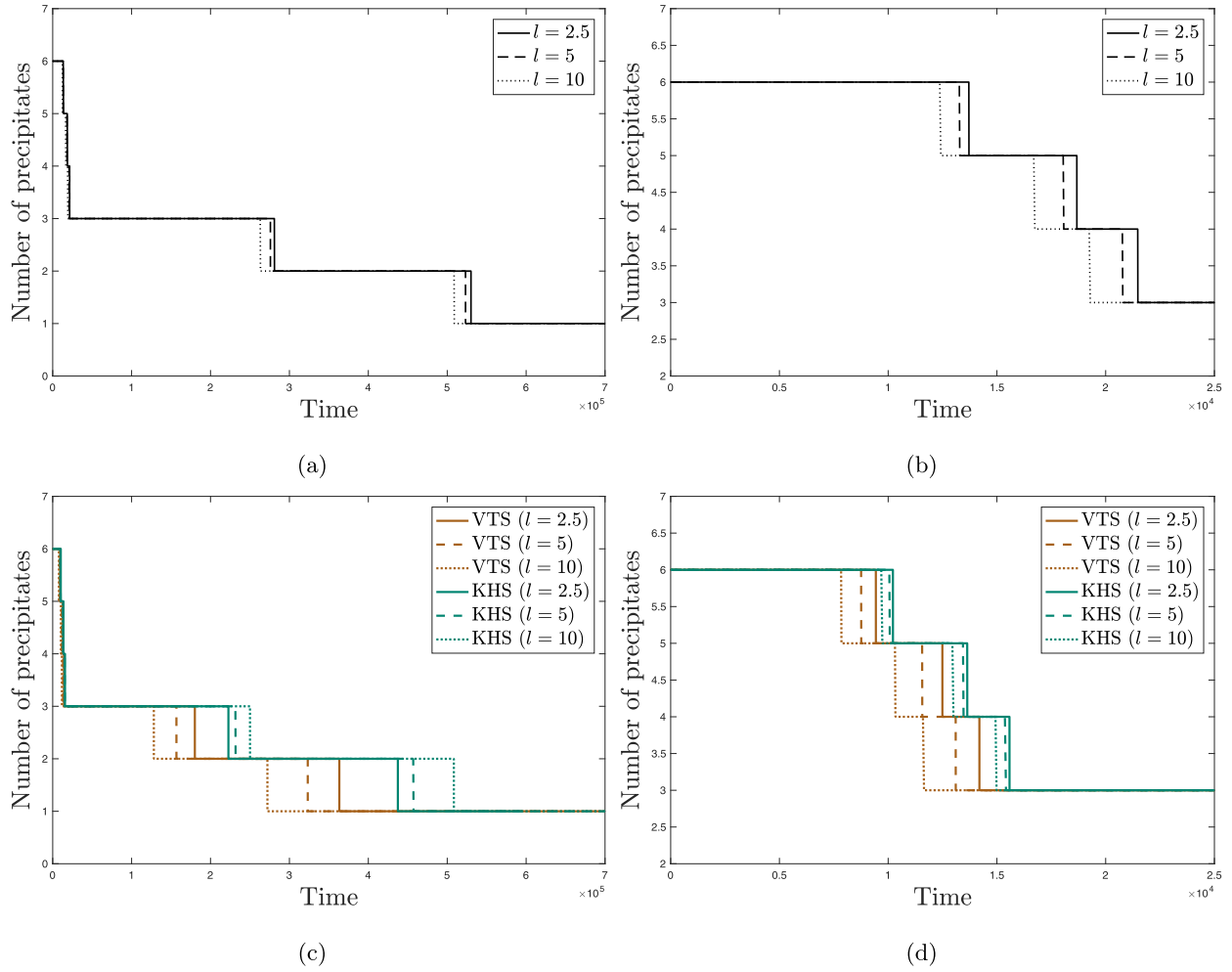
Fig. 5. Evolution of the number of precipitates predicted by the model without elasticity (a, b), and the models coupled with the KHS and VTS schemes(c, d). (a) and (c) shows the evolution of the number of precipitates during the whole simulations, while (b) and (d) focuses on the early stages of the simulation. The kinetics of the microstructure evolution is affected by the choice of elastic scheme, with the microstructure evolution predicted by the KHS model being consistently slower than the one predicted with the VTS model in this study. As observed in Fig. 4, for an interfacial length equal to $l = 10$, VTS predicts a microstructure with 3 particles at $t = 11723$, while KHS still predicts 5 particles at $t = 13002$, and 4 particles until $t = 14934$. As the interfacial thickness increases, the difference between the two models increases as well. As expected, as interfacial thickness decreases, the predictions of both models converge. Moreover, the differences due to the interfacial length in (a) and (b) are aggravated by the VTS model, and reduced or even reversed by the KHS scheme.
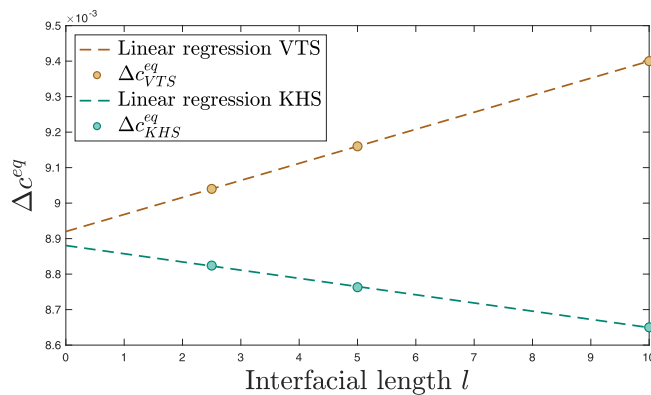
Fig. 6. Evolution of the shift in equilibrium concentrations Δc^{eq} as a function of the interfacial length l for both the KHS and VTS models. As expected, Δc^{eq}_{VTS} increases as l increases due to the positive excess elastic energy, while Δc^{eq}_{KHS} decreases as l increases due to the negative excess elastic energy. When l decreases towards 0, Δc^{eq}_{VTS} and Δc^{eq}_{KHS} seem to converge towards $\Delta c^{eq} = 8.9 \times 10^{-3}$, which thus corresponds to the shift in concentration due to the presence of elasticity predicted due to the Gibbs-Thompson effect.

Fig. 5c and d). In both Fig. 5c and d, it is possible to see that for a fixed interfacial length, the dissolution is quicker with the VTS than with the KHS model. Moreover, it is interesting to see that the excess elastic energy at the interface impacts the effective interfacial length of the system. When the model parameters are defined to fix $l = 10$ following Eq. (5), the equilibrium microstructures shown in Fig. 4e and f have an interfacial length of $l^{VTS} = 8.4 < l$ and $l^{KHS} = 14.5 > l$, respectively. This is because a positive excess elastic energy increases the constraints on the interface of the system, while a negative excess elastic energy artificially relaxes these constraints, leading to a greater interfacial length with the KHS model than with the VTS when the contribution from this excess energy is significant. This, as will be discussed later, leads to even greater differences between the two models.

In addition to changing the kinetics and the effective interfacial energy, the elastic scheme influences the equilibrium microstructure by changing the elastic contribution to the model. As Cahn and Larché mentioned in [43], the elastic energy term modifies the equilibrium concentrations of the phases involved from the equilibrium predicted by chemistry alone. This concentration shift explains in part the different kinetics between the elastic-free model and the other two, which can be seen when comparing Fig. 5a with c and Fig. 5b with d. However, since the VTS and the KHS introduce an excess elastic energy at

the interface, they both lead to an artificial additional shift in the equilibrium concentration in addition to the shift due to elasticity alone. As shown in Fig. 6, in this study, the simulations presented in Fig. 4e and f show a positive shift equal to $\Delta c_{VTS}^{eq} = 9.45 \times 10^{-3}$ for the VTS scheme, and equal to $\Delta c_{KHS}^{eq} = 8.65 \times 10^{-3}$ for the KHS scheme compared to equilibrium concentrations predicted from the chemistry of the system alone, presented in Table 1 ($c_\alpha^{eq} = 0.1$ and $c_\beta^{eq} = 0.9$). As stated earlier, these shifts correspond to the sum of the expected shift due to the elastic energy with the shift due to the excess elastic energy introduced. These shifts lead to different predictions for the equilibrium size of the precipitate. Furthermore, the particle size, in turn, influences the elastic contribution to the system, shifting the equilibrium concentration further.

As interfacial length increases, the contribution of these two effects, namely the impact of the elastic scheme on the interfacial energy and the elastic contribution, become more important, and affect both kinetics and equilibrium microstructure. To understand the effect of the interface length on the models' kinetics, it is first important to understand the effect that the interfacial length has on kinetics without elasticity. When no elasticity is added to this model, a longer interfacial length leads to quicker dissolution kinetics, as shown in Fig. 5a and b. This is because modifying κ and m changes the value of χ introduced in Eq. (19) and defined in Eq. (20) and of the driving force in Eq. (21). In this study, the interfacial length l is changed while keeping the interfacial energy σ constant. As l increases, $m = \frac{2\sqrt{2}}{l}$ decreases and $\kappa = \frac{1}{m}$ increases to keep $\sigma = \frac{\sqrt{2}}{3}$. As a result, in Eq. (20), the term $\frac{\partial^2 \omega_{bulk}}{\partial \mu^2}$ decreases and the term $\frac{\partial^2 \omega_{grad}}{\partial \mu^2}$ increases. Similarly, in Eq. (19), the term $\frac{\partial \omega_{bulk}}{\partial \eta}$ decreases while the term $\frac{\partial \omega_{grad}}{\partial \eta}$ increases. These changes influence the evolution kinetics, which in this case, lead to a quicker dissolution for higher interfacial lengths, even without elastic contribution. In addition to this effect, the introduction of elastic schemes in the phase field model leads to greater differences between simulations with different interfacial lengths. As shown in Fig. 3, the magnitude of the excess of energy at the interface introduced by the elastic models is a function of the interfacial length. As a result, as the interfacial length increases, the VTS model will tend to dissolve quicker, while the KHS model will tend to predict slower dissolution. As shown in Fig. 5c and d, when using the VTS model, dissolution simulations with a larger interfacial length, which already had a high effective kinetic parameter L as discussed above, become even quicker because of the positive excess energy at the interface. When using the KHS model, the higher dissolution kinetics for larger interfacial lengths are reduced, or even reversed by the negative excess elastic energy, as shown in Fig. 5c and d. The reason why the KHS scheme only reduces the difference at the early stages of the simulation and reverses them later is that the microstructure evolution is initially governed by the chemical driving force, whereas the contribution from the interfacial energy becomes more important only later. Moreover, Fig. 5c and d shows that as the interfacial length decreases, the magnitude of the excess elastic energy decreases, and the difference between the predictions of the VTS and the KHS model decreases as well. As the interfacial length converges towards 0, the models' predictions converge towards a solution without any excess of energy at the interface.

In addition to its effect on evolution kinetics, changing the interfacial length also affects the equilibrium microstructure. In particular, as shown in Fig. 6, the shift in equilibrium concentration depends linearly on the interfacial length. This shift increases with increasing interfacial length with the VTS model due to the positive excess elastic energy, and decreases with increasing interfacial length with the KHS model due to the negative excess elastic energy. This leads to greater error in model prediction as the interfacial length increases. It is interesting to note that the shift in equilibrium composition can be decoupled in the two parts described above: the Gibbs-Thompson effect and the shift due to the excess of elastic energy. As the interfacial length

decreases, the two linear regressions for the VTS and KHS models shown in Fig. 6 converge towards $\Delta c^{eq} = 8.9 \times 10^{-3}$, which corresponds to the shift in equilibrium concentration without excess elastic energy predicted by the Gibbs-Thompson effect. The rest of the shift, positive for the VTS model, and negative for the KHS model, corresponds to the shift due to the excess elastic energy.

Microstructure evolution depends strongly on the choice of elastic scheme, especially when the contribution of the excess elastic energy becomes significant. This means that when the elastic constants, the eigenstrain values, and the interfacial thickness are large, or when the interfacial energy is small, the choice of elastic scheme affects the phase field predictions. The different elastic schemes predict different kinetics, different equilibrium compositions, different interfacial energy, and different effective interfacial length. As a result, it is recommended to limit the interfacial length when possible and favor the KHS model over the VTS model to limit the undesired effects of the elastic scheme on microstructure evolution.

5. Additional note on a limitation of the grand potential model

In his paper, Plapp described the development of a grand potential model and showed the equivalence with a WBM phase field model based on the total energy functional [14]. The system being studied includes the energy contributions from the bulk, the interface, and the chemistry of the phases. One of the main limitations described in his publication is the need for an explicit and invertible expression between the chemical potential and the composition. In general, such an explicit and invertible expression is required between the total potential and the concentration to account for the contribution of other sources of energy in the system.

For the expression to be invertible, the total free energy density f_{tot} has to be a convex function of the composition. This ensures that the relation between the total potential provided by

$$\mu = \frac{\partial f_{tot}}{\partial \rho}. \tag{23}$$

and the concentration c is monotonous and thus invertible.

The conditions expressed in [14] can be derived by having the total free energy equal to the sum of the chemical contribution f_{chem} and the interfacial contribution f_{int} such that $f_{tot} = f_{chem} + f_{int}$. In that case, if f_{int} is independent of the concentration (no square gradient terms in c), then Eq. (23) becomes

$$\mu = \frac{\partial (f_{chem} + f_{int})}{\partial \rho} = \frac{\partial f_{chem}}{\partial \rho} + \frac{\partial f_{int}}{\partial \rho} = \frac{\partial f_{chem}}{\partial \rho} = \mu_{chem}, \tag{24}$$

which shows that the condition on f_{tot} becomes a condition on f_{chem} alone.

However, if the system includes another concentration-dependent energy contribution, such as elastic energy f_{el}, Eq. (23) becomes

$$\mu = \frac{\partial (f_{chem} + f_{int} + f_{el})}{\partial \rho} = \frac{\partial f_{chem}}{\partial \rho} + \frac{\partial f_{el}}{\partial \rho}. \tag{25}$$

It is important to note, however, that f_{tot} being convex only ensures that there is an invertible relation between the total potential μ and the concentration c. For the relation to be explicit, which is necessary to have a solvable system linking c to μ, the conditions on the composition-dependency of f_{el} can be quite restrictive and depend on the system being studied. This difficulty can be avoided by introducing in the system of equations of the model an equation to solve Eq. (25) for the concentration c. However, numerical complications could arise.

These conditions can make it challenging to introduce some physics into a grand potential model. For example, it is difficult to properly introduce the strain due to the presence of solute atoms in the matrix. In phase field models, this strain could be added to the model in several ways. One way, when using the KHS scheme, could be to define ϵ_α^* as

$$\epsilon_{ij,\alpha}^* = \epsilon_{ij,\alpha}^{*,1} + c\ \ \epsilon_{ij,\alpha}^{*,2}, \tag{26}$$

with $\epsilon_{ij,\alpha}^{*,1}$ and $\epsilon_{ij,\alpha}^{*,2}$ independent of the concentration c. This expression of the eigenstrain would then go into Eq. (16) and make the elastic energy defined in Eq. (17) concentration-dependent. However, in the context of the grand potential model, ensuring that f_{el} is convex and that the relation between the total potential μ and the concentration c is explicit can lead to restrictions on the shape of the stiffness tensors $C_{ijkl,\alpha}$ and the eigenstrain components $\epsilon_{ij,\alpha}^{*,1}$ and $\epsilon_{ij,\alpha}^{*,2}$. This limitation might disqualify the use of the grand potential model for certain studies.

6. Conclusion

Two grand potential models coupled with different elastic interpolation models have been developed in MOOSE. The performance of these models has been evaluated by comparing their results to analytical solutions in two different configurations. The VTS model, an energy interpolation, introduces a large positive excess elastic energy at the interface, while the KHS model, an interpolation of elastic properties, introduces a negative excess elastic energy contribution, generally smaller in magnitude than the VTS model. Besides, this study provides an evaluation of the magnitude of the excess energy introduced by elastic schemes, and it has been shown to proportionally decrease towards zero with the interfacial thickness.

Moreover, it was shown that morphology evolution predicted by the grand potential models coupled with elastic schemes depends strongly on the choice of the elastic model when the contribution of the excess energy becomes significant. When choosing the interfacial length to resolve the microstructure while limiting the computational cost of the simulation, it is also important to consider the contribution of the excess elastic energy at the interface. Authors thus suggest limiting the interfacial length and recommend the use of the KHS model over the VTS model to limit the artificial effect of the elastic scheme on microstructure evolution kinetics, interfacial energy, interfacial length, and equilibrium microstructure.

The paper also exposes one potential limitation of the grand potential model. Since an explicit and invertible relation has to link the total potential and the composition, the introduction of a composition-dependent elastic contribution in the model can be challenging.

Data availability

The MOOSE grand potential phase field model input files used to run the simulations are available to download in the 'Research Data' Section. The MOOSE source code can be obtained from http://mooseframework.org/.

CRediT authorship contribution statement

Larry K. Aagesen: Supervision, Conceptualization, Methodology, Writing - review & editing, Funding acquisition, Resources. **Arthur T. Motta:** Supervision, Writing - review & editing, Funding acquisition. **Michael R. Tonks:** Supervision, Conceptualization, Writing - review & editing.

Declaration of Competing Interest

The authors declare that they have no known competing financial interests or personal relationships that could have appeared to influence the work reported in this paper.

Acknowledgments

References

[1] L.Q. Chen, Phase-field models for microstructure evolution, Annu. Rev. Mater. Res. 32 (2002) 113–140.

[2] N. Moelans, B. Blanpain, P. Wollants, An introduction to phase-field modeling of microstructure evolution, Calphad 32 (2008) 268–294.

[3] I. Steinbach, Phase-field models in materials science, Modell. Simul. Mater. Sci. Eng. 17 (2009) 073001 .

[4] C.E. Krill, Phase-field modeling of grain growth, Handbook of Materials Modeling, Springer, Netherlands, Dordrecht, 2005.

[5] N. Moelans, B. Blanpain, P. Wollants, Quantitative analysis of grain boundary properties in a generalized phase field model for grain growth in anisotropic systems, Phys. Rev. B 78 (2008) 024113 .

[6] N. Moelans, F. Wendler, B. Nestler, Comparative study of two phase-field models for grain growth, Comput. Mater. Sci. 46 (2009) 479–490.

[7] R. Spatschek, E. Brener, A. Karma, Phase field modeling of crack propagation, Philos. Mag. 91 (2011) 75–95.

[8] P. Chakraborty, Y. Zhang, M.R. Tonks, Multi-scale modeling of microstructure dependent intergranular brittle fracture using a quantitative phase-field based method, Comput. Mater. Sci. 113 (2016) 38–52.

[9] N.P. Mitchell, V. Koning, V. Vitelli, W. Irvine, Fracture in sheets draped on curved surfaces, Nat. Mater. 16 (2017) 89–93.

[10] F.T. Huang, F. Xue, B. Gao, L.H. Wang, X. Luo, et al., Domain topology and domain switching kinetics in a hybrid improper ferroelectric, Nat. Commun. 7 (2016) 11602.

[11] T. Koyama, Phase-field modeling of microstructure evolutions in magnetic materials, Sci. Technol. Adv. Mater. 9 (2008) 013006 .

[12] M.R. Tonks, L.K. Aagesen, The phase field method: mesoscale simulation aiding material discovery, Annu. Rev. Mater. Res. (2019) 49:annur-ev–matsci–070218–010151.

[13] A.A. Wheeler, W.J. Boettinger, G.B. McFadden, Phase-field model for isothermal phase transitions in binary alloys, Phys. Rev. A 45 (1992) 7424–7439.

[14] M. Plapp, Unified derivation of phase-field models for alloy solidification from a grand-potential functional, Phys. Rev. E 84 (2011) 031601 .

[15] L.K. Aagesen, Y. Gao, D. Schwen, K. Ahmed, Grand-potential-based phase-field model for multiple phases, grains, and chemical components, Phys. Rev. E 98 (2018) 023309 .

[16] A. Choudhury, B. Nestler, Grand-potential formulation for multicomponent phase transformations combined with thin-interface asymptotics of the double-obstacle potential, Phys. Rev. E 85 (2012).

[17] J. Hötzer, M. Jainta, P. Steinmetz, B. Nestler, A. Dennstedt, et al., Large scale phase-field simulations of directional ternary eutectic solidification, Acta Mater. 93 (2015) 194–204.

[18] P. Steinmetz, M. Kellner, J. Hötzer, A. Dennstedt, B. Nestler, Phase-field study of the pattern formation in Al-Ag-Cu under the influence of the melt concentration, Comput. Mater. Sci. 121 (2016) 6–13.

[19] P. Steinmetz, J. Hötzer, M. Kellner, A. Genau, B. Nestler, Study of pattern selection in 3D phase-field simulations during the directional solidification of ternary eutectic Al-Ag-Cu, Comput. Mater. Sci. 148 (2018) 131–140.

[20] M. Kellner, I. Sprenger, P. Steinmetz, J. Hötzer, B. Nestler, M. Heilmaier, Phase-field simulation of the microstructure evolution in the eutectic NiAl-34Cr system, Comput. Mater. Sci. 128 (2017) 379–387.

[21] Y.C. Yabansu, P. Steinmetz, J. Hötzer, S.R. Kalidindi, B. Nestler, Extraction of reduced-order process-structure linkages from phase-field simulations, Acta Mater. 124 (2017) 182–194.

[22] K. Dargahi Noubary, M. Kellner, P. Steinmetz, J. Hötzer, B. Nestler, Phase-field study on the effects of process and material parameters on the tilt angle during directional solidification of ternary eutectics, Comput. Mater. Sci. 138 (2017) 403–411.

[23] S.G. Kim, W.T. Kim, T. Suzuki, Phase-field model for binary alloys, Phys. Rev. E 60 (1999) 7186–7197.

[24] A. Durga, P. Wollants, N. Moelans, Evaluation of interfacial excess contributions in different phase-field models for elastically inhomogeneous systems, Modell. Simul. Mater. Sci. Eng. 21 (2013) 055018 .

[25] A. Durga, P. Wollants, N. Moelans, A quantitative phase-field model for two-phase

elastically inhomogeneous systems, Comput. Mater. Sci. 99 (2015) 81–95.

[26] L.K. Aagesen, D. Schwen, K. Ahmed, M.R. Tonks, Quantifying elastic energy effects on interfacial energy in the Kim-Kim-Suzuki phase-field model with different interpolation schemes, Comput. Mater. Sci. 140 (2017) 10–21.

[27] K. Ammar, B. Appolaire, G. Cailletaud, S. Forest, Combining phase field approach and homogenization methods for modelling phase transformation in elastoplastic media, Revue européenne de mécanique numérique 18 (2009) 485–523.

[28] Armen G. Khachaturyan, Theory of Structural Transformations in Solids, Wiley, New York, 1983 available at: https://scholar.google.com/scholar_lookup?title= Theory%20of%20Structural%20Transformations%20in%20Solids&publication_ year=1983&author=A.G.%20Khachaturyan.

[29] D.Y. Li, L.Q. Chen, Computer simulation of morphological evolution and rafting of γ' particles in Ni-based superalloys under applied stresses, Scr. Mater. 37 (1997) 1271–1277.

[30] I. Steinbach, M. Apel, Multi phase field model for solid state transformation with elastic strain, Physica D 217 (2006) 153–160.

[31] S.Y. Hu, L.Q. Chen, A phase-field model for evolving microstructures with strong elastic inhomogeneity, Acta Mater. 49 (2001) 1879–1890.

[32] P. Yu, S.Y. Hu, L.Q. Chen, Q. Du, An iterative-perturbation scheme for treating inhomogeneous elasticity in phase-field models, J. Comput. Phys. 208 (2005) 34–50.

[33] G.I. Tóth, Phase-field modeling of isothermal quasi-incompressible multicomponent liquids, Phys. Rev. E 94 (2016) 033114 .

[34] P.C. Bollada, P.K. Jimack, A.M. Mullis, Multiphase field modelling of alloy solidification, Comput. Mater. Sci. 171 (2020) 109085 .

[35] N. Moelans, A quantitative and thermodynamically consistent phase-field interpolation function for multi-phase systems, Acta Mater. 59 (2011) 1077–1086.

[36] J.W. Cahn, S.M. Allen, A microscopic theory for domain wall motion and its experimental verification in Fe-Al alloy domain growth kinetics, Le Journal de Physique Colloques (1977) 38:C7–51–C7–54.

[37] M.R. Tonks, D. Gaston, P.C. Millett, D. Andrs, P. Talbot, An object-oriented finite element framework for multiphysics phase field simulations, Comput. Mater. Sci. 51 (2012) 20–29.

[38] D. Schwen, L.K. Aagesen, J.W. Peterson, M.R. Tonks, Rapid multiphase-field model development using a modular free energy based approach with automatic differentiation in MOOSE/MARMOT, Comput. Mater. Sci. 132 (2017) 36–45.

[39] C.J. Permann, D.R. Gaston, D. Andrš, R.W. Carlsen, F. Kong, et al., MOOSE: enabling massively parallel multiphysics simulation, SoftwareX 11 (2020).

[40] D. Gaston, C. Newman, G. Hansen, D. Lebrun-Grandié, MOOSE: a parallel computational framework for coupled systems of nonlinear equations, Nucl. Eng. Des. 239 (2009) 1768–1778.

[41] X. Jin, L.M. Keer, Q. Wang, A closed-form solution for the Eshelby tensor and the elastic field outside an elliptic cylindrical inclusion, J. Appl. Mech. 78 (2011) 031009 .

[42] P.W. Voorhees, W.C. Johnson, The thermodynamics of elastically stressed crystals, Solid State Physics – Advances in Research and Applications, vol. 59, Academic Press Inc., 2004, p. 59.

[43] J.W. Cahn, F. Larché, A simple model for coherent equilibrium, Acta Metall. 32 (1984) 1915–1923.